Supplementary materials for: Direct observation of topological magnon edge states

Jihai Zhang[1,2]†, Meng-Han Zhang[1,2]†, Peigen Li[1,2]†, Zizhao Liu[1,2], Ye Tao[1,2], Hongkun Wang[1,2], Dao-Xin Yao[1,2]*, Donghui Guo[1], and Dingyong Zhong[1,2]*

[1]School of Physics & Guangdong Provincial Key Laboratory of Magnetoelectric Physics and Devices; Sun Yat-sen University, 510275 Guangzhou, China

[2]State Key Laboratory of Optoelectronic Materials and Technologies, Sun Yat-sen University, 510275 Guangzhou, China

*Corresponding author. Email: dyzhong@mail.sysu.edu.cn (D.Z.); yaodaox@mail.sysu.edu.cn (D.-X.Y.)

†The authors equally contributed to this work.

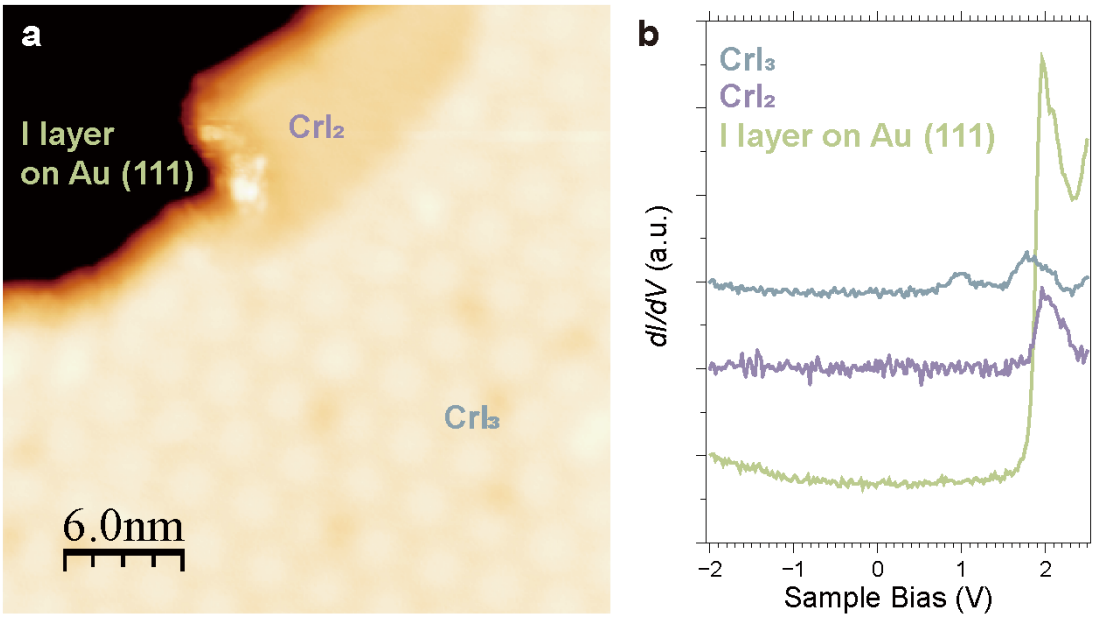

Supplementary Figure 1. STM(S) of CrI_3/CrI_2 monolayers and iodine passivation layer on Au(111). a, STM image (setpoint: 2.0 V, 10 pA). **b**, STS curves from CrI_3, CrI_2 and the iodine passivation layer showing an insulating feature (setpoint: -2.0 V, 100 pA).

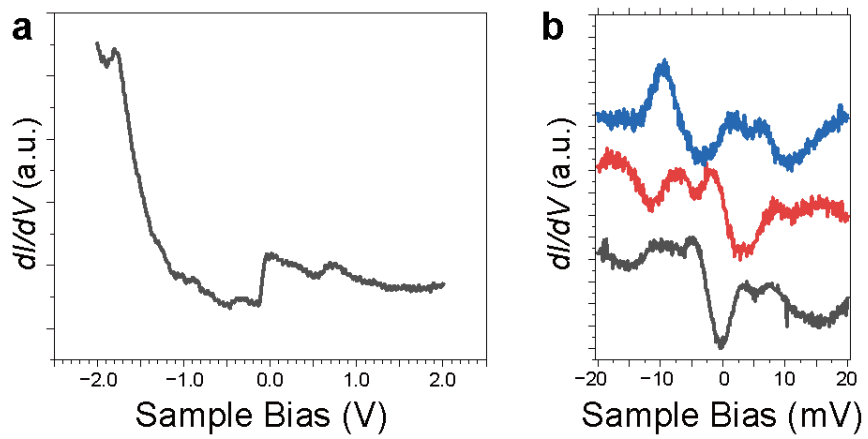

Supplementary Figure 2. Verification of tip conditions. a, Typical STS curve from Ag(111) showing the step of Shockley surface states at −0.05 V. **b**, STS results in the range from –20 to 20 mV on Ag(111), showing position-dependent non-symmetric peaks from the interference of the Ag(111) surface states.

Supplementary Text

IETS results on different position in the CrI_3 island

As shown in Supplementary Fig. 3a below, the CrI_3 has a moiré pattern on Au(111) surface, which may introduce extra moiré potential into the system and lead to extra peaks to the magnon bands.[1] As shown in Supplementary Fig. 3b, IETS are taken at different positions. The raw data are shown in Supplementary Fig. 3c. All IETS results show a symmetric behavior, without significant difference. In all results, the plateau like signal can be clearly seen, although different lines may have slight differences in the signal strength. A symmetric normalization was performed to help focus on the symmetric signals.

$$\frac{dI}{dV}(V)_{symm} = \frac{dI}{dV}(V)_{raw} + \frac{dI}{dV}(-V)_{raw}$$

The normalized results (circles, Supplementary Fig. 3d) were further smoothed by means of the lowess method (color lines). To further explore the details of the excitation density of states, a numerical differentiation were carried out. As shown in Supplementary Fig. 3e, the numerical d^2I/dV^2 results exhibit similar shapes. Other IETS results in this work were analyzed with the same method.

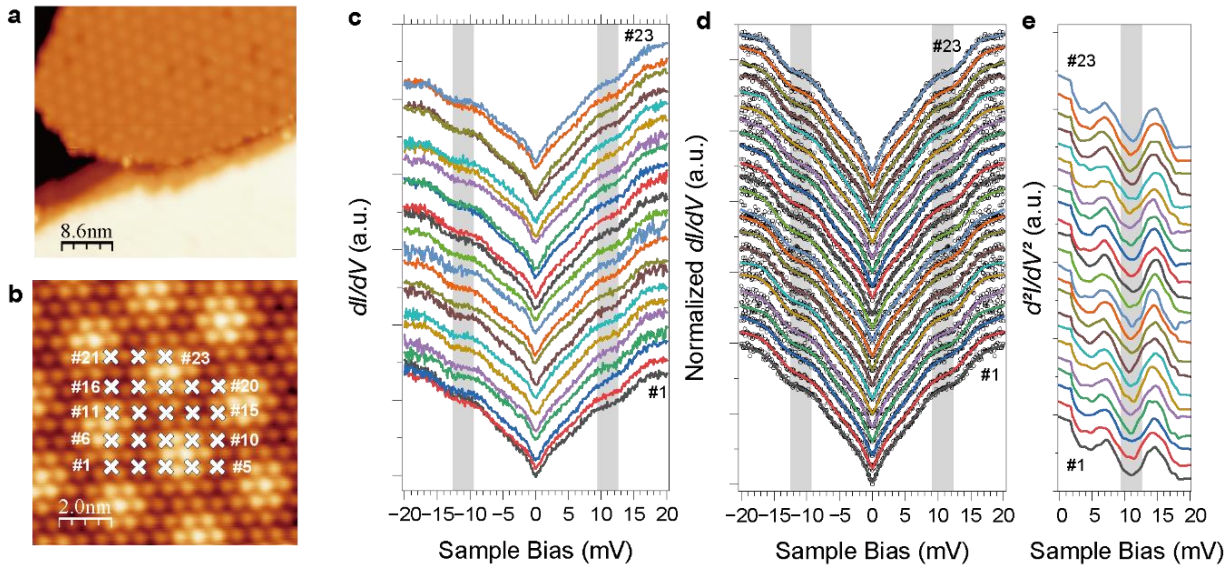

Supplementary Figure 3. IETS at different positions in CrI_3 island center. a, STM image of a CrI_3 island (setpoint: 2.0 V, 10 pA). **b**, Zoom-in STM image (setpoint: 2.0 V, 100 pA). Positions for the STS measurements in c are marked by crosses. **c**, STS results inside the CrI_3 island. (Setpoint: 20 mV, 200 pA, modulation: 926 Hz, 0.5 mV) **d**, Symmetrized normalization (circles) and smoothed (lines) results of the raw STS in c. **e**, d^2I/dV^2 results from numerical differentiation on the smoothed dI/dV results in d.

Additional IETS results with magnetic-field dependence

We have conducted field-dependent measurements of magnon spectra on different sample islands. All results (shown in Supplementary Fig. 4) exhibit the Zeeman-like energy shift in an out-of-plane magnetic field.

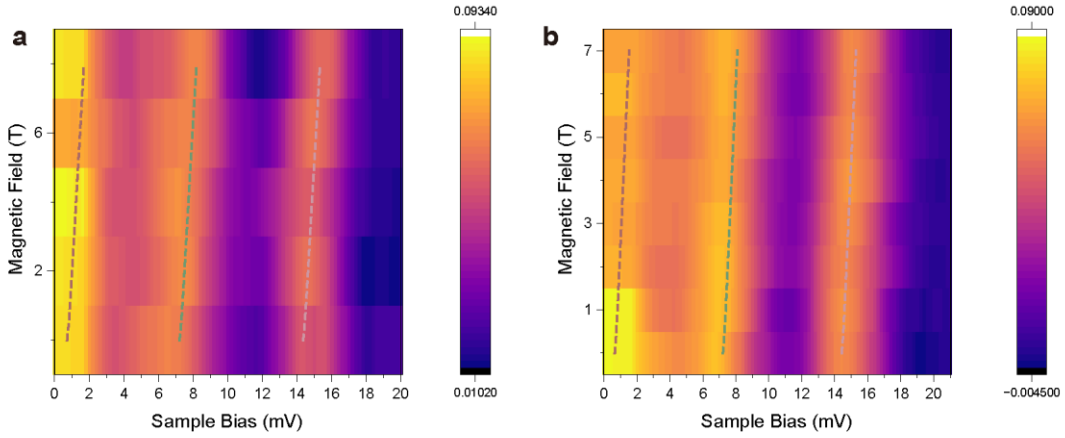

Supplementary Figure 4. Additional magnetic-field dependent IETS. The results show two field dependent results on different sample islands. The dotted lines are the theoretical results shown in Fig. 2b.

More about IETS across topological edges

To rule out other possible topological trivial origin of the boundary states like dangling bonds or merging effect from both sides of the boundary, we took IETS measurements across various topological edges. The position of the line spectra and the raw data of Fig. 3 in the main text are shown in Supplementary Fig. 5 below.

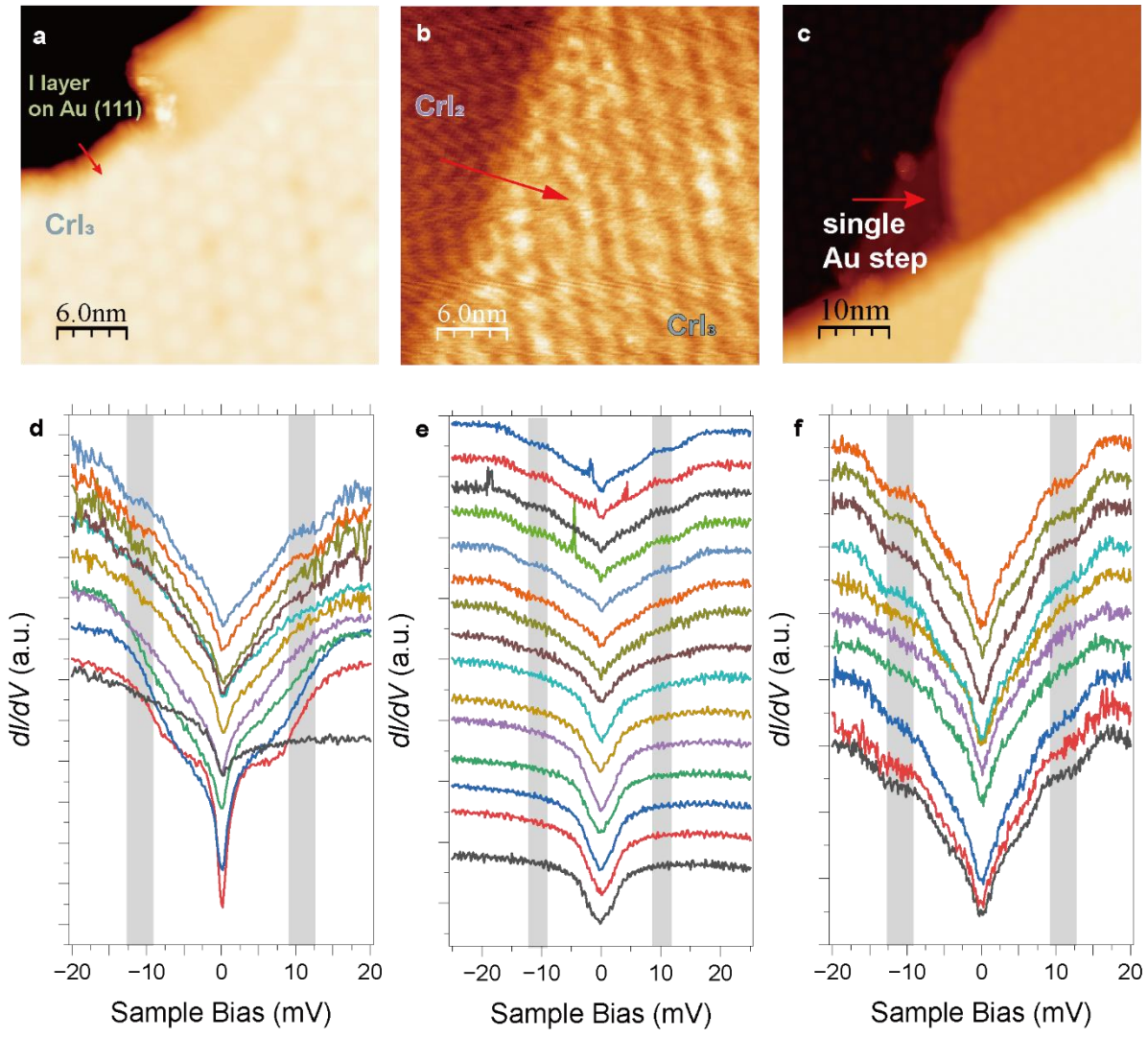

Supplementary Figure 5. STM images and raw STS data of the measurements shown in main text Fig. 3. a, STM image showing the position of the line spectra in Fig. 3b across a CrI_3 island (setpoint: 2.0 V, 10 pA). **b**, STM image showing the position of the line spectra in Fig. 3c across

a CrI_3-CrI_2 boundary (setpoint: 2.5 V, 10 pA). **c**, STM image showing the position of the line spectra in Fig. 3d across CrI_3 covered Au(111) step edge (setpoint: 2.0 V, 10 pA).**d**, Raw IETS data of Fig. 3b. **e**, Raw IETS data of Fig.3c. **f**, Raw IETS data of Fig. 3d.

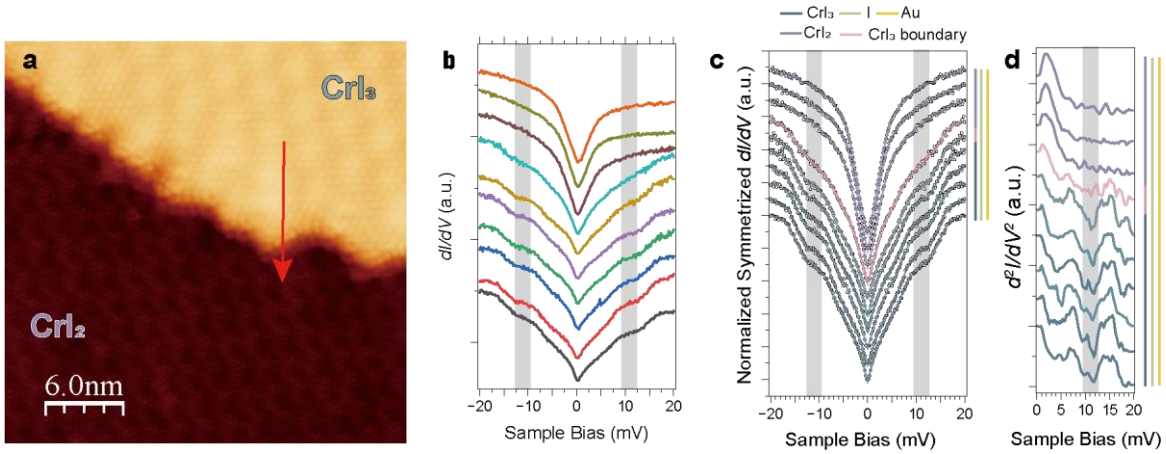

Supplementary Figure 6. Additional IETS across the CrI_3-CrI_2 boundary. a, STM image of the region for the IETS measurements (setpoint: 1.0 V, 50 pA). The position of the line spectra is shown by the red arrow. **b**, Raw data of the line spectra. **c**, The symmetrized normalization of the *dI/dV* results shown in b. the smoothed results are shown in color lines. **d**, Numerical differentiation results of the lines shown in c.

Theoretical Model

1. Band Topology

We map the original spin Hamiltonian to a bosonic tight binding model via the higher order Holstein-Primakoff (HP) representation to study the magnetic excitations.

$$S^+ = \sqrt{2S}\left(a - \frac{a^\dagger a a}{4S}\right), S^- = \sqrt{2S}\left(a^\dagger - \frac{a^\dagger a^\dagger a}{4S}\right), S^z \approx S - a^\dagger a.$$

After the Fourier transformation, the Hamiltonian in reciprocal space is given by

$$H^0(\boldsymbol{k}) = S(3J_1 + 6J_2 + 3J_3 + h_B + 2K - J_2\gamma_2)\boldsymbol{\sigma_0} + S\boldsymbol{d_k}\cdot\boldsymbol{\sigma}$$

where $\boldsymbol{\sigma_0}$ is identity matrix, $\boldsymbol{\sigma} = (\sigma_x, \sigma_y, \sigma_z)$ are Pauli matrices, and $\boldsymbol{d_k} = (d_x, d_y, d_z)$ with $d_x = -J_1\gamma_1 - J_3\gamma_3$, $d_y = -J_1\gamma_1' - J_3\gamma_3'$ and $d_z = -D_z\gamma_{D_z}$. Here, the related coefficients are given by

$$\gamma_1 = cos(k_y) + 2cos\left(\frac{\sqrt{3}}{2}k_x\right)cos\left(\frac{k_y}{2}\right),$$

$$\gamma_1' = -sin(k_y) + 2cos\left(\frac{\sqrt{3}}{2}k_x\right)sin\left(\frac{k_y}{2}\right),$$

$$\gamma_2 = 2cos(\sqrt{3}k_x) + 4cos\left(\frac{\sqrt{3}}{2}k_x\right)cos\left(\frac{3k_y}{2}\right),$$

$$\gamma_3 = cos(2k_y) + 2cos(\sqrt{3}k_x)cos(k_y),$$

$$\gamma_3' = sin(2k_y) - 2cos(\sqrt{3}k_x)sin(k_y),$$

$$\gamma_{D_z} = 2sin(\sqrt{3}k_x) - 4sin\left(\frac{\sqrt{3}}{2}k_x\right)cos\left(\frac{3k_y}{2}\right).$$

The magnon bands of the model can be obtained analytically as

$$\omega_k^{\pm} = S(3J_1 + 6J_2 + 3J_3 + h_B + 2K - J_2\gamma_2) \pm S\sqrt{{d_x}^2 + {d_y}^2 + {d_z}^2}.$$

The calculated band structures are shown below in Supplementary Fig. 7.

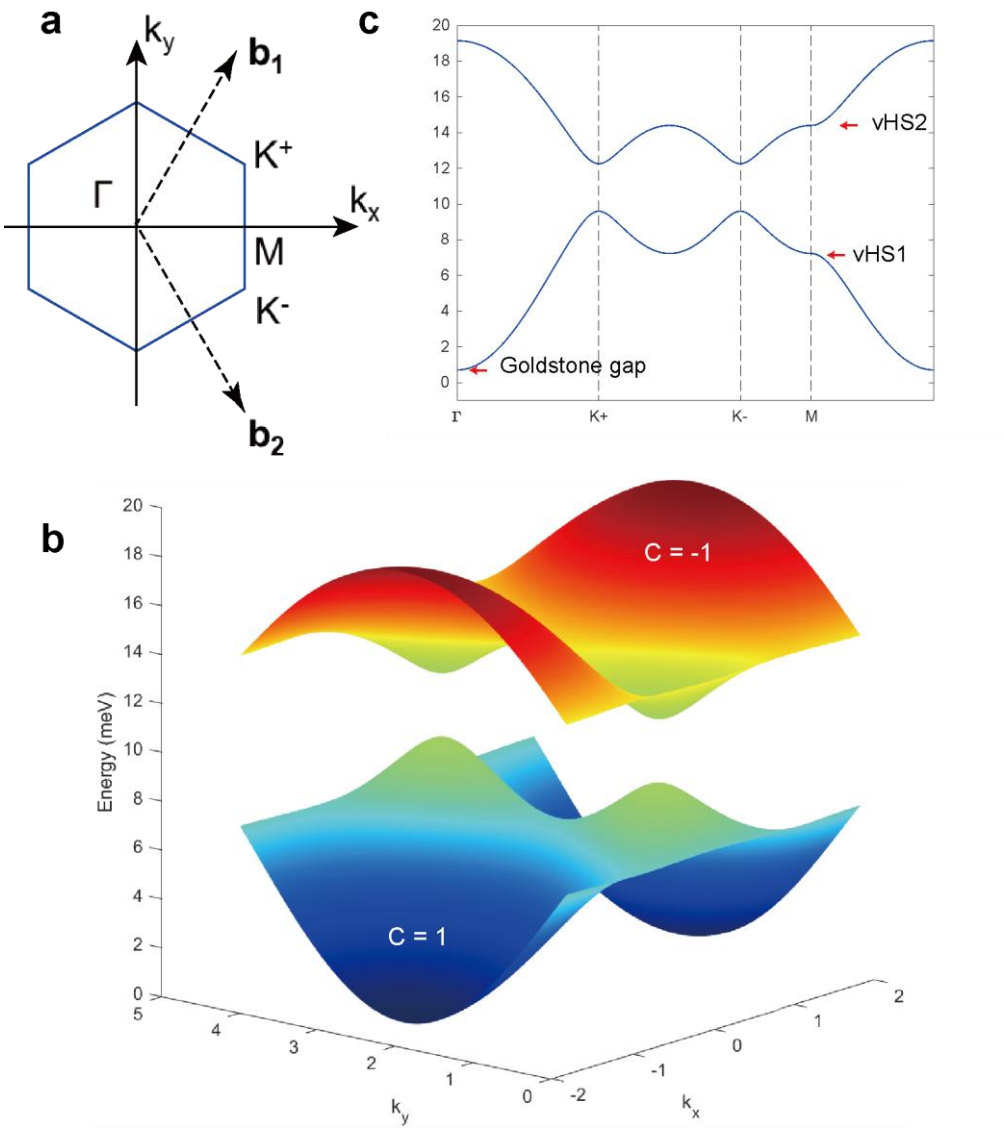

95

96 **Supplementary Figure 7. Magnon Chern insulator from the theoretical model of two-**
97 **dimensional honeycomb lattice. a**, The first Brillouin zone with high symmetry points, where b_1
98 and b_2 are basis vectors of reciprocal space. **b**, Magnon dispersion with $J_1 = 2.12\,meV$.
99 Parameters choices are $J_2 = 0.15\,J_1$, $J_3 = -0.04\,J_1$, $D_z = 0.08\,J_1$ $K = 0.12\,J_1$ and $h_B = 0$. **c**, The
100 magnon bands of honeycomb lattice along $\Gamma - K^+ - K^- - M - \Gamma$, where the Goldstone gap and
101 two von Hove singularities are marked by red arrows.

102

The fourfold degeneracy at the $K^{\pm} = \left(\frac{2\pi}{3}, \pm\frac{2\pi}{3\sqrt{3}}\right)$ points is a manifestation of the Dirac linear dispersion relation, which is protected by the lattice symmetry and time-reversal symmetry. We project the magnon bands onto the subspace around the crossings introducing an effective Hamiltonian

$$H^{eff}(\boldsymbol{k}) = S(3J_1 + 6J_2 + 3J_3 + h_B + 2K)\boldsymbol{\sigma_0} \pm 3\sqrt{3}D_z S\sigma_z + \left(\frac{3}{2}J_1 - 3J_3\right)S\left(k_x\sigma_y \pm k_y\sigma_x\right).$$

We define $\boldsymbol{d_k^{eff}} = \left(\frac{3}{2}J_1S - 3J_3S, \frac{3}{2}J_1S - 3J_3S, 3\sqrt{3}D_zS\right)$, which is a linear combination of Pauli matrices in the restricted subspace. Due to the typically weak DMI, the distribution of Berry curvature $\Omega_k^{\pm}$ is maintly concentrated around the Dirac point displayed in Supplementary Fig. 8.

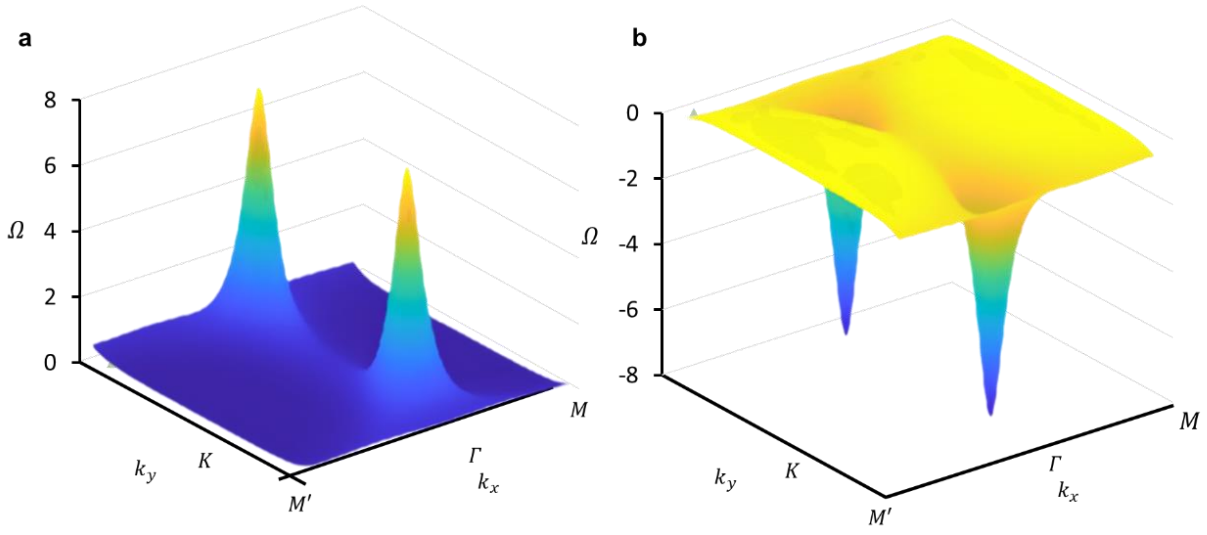

Supplementary Figure 8. Schematics of the band topology. a, Berry curvature of the bottom band. **b**, Berry curvature of the top band. The corresponding Chern numbers are ± 1.

For the single Dirac crossing, the symbolic function $\mp \mathrm{sgn}(D_z)$ can effectively capture the intrinsic topology corresponding to valley degrees of freedom. We obtain the analytical solution of the Chern number $\mathrm{C}^{\pm}$

$$C^{\pm} = \mp \frac{1}{4\pi} \iint_{BZ} dk_x dk_y \frac{\boldsymbol{d}_{\boldsymbol{k}}^{\boldsymbol{eff}} \cdot \left(\partial_{k_x} \boldsymbol{d}_{\boldsymbol{k}}^{\boldsymbol{eff}} \times \partial_{k_y} \boldsymbol{d}_{\boldsymbol{k}}^{\boldsymbol{eff}} \right)}{2 \left| \boldsymbol{d}_{\boldsymbol{k}}^{\boldsymbol{eff}} \right|^3}$$

2. Magnon-Magnon interactions

To include the magnon-magnon interactions, we rewrite the next-nearest neighbors and the anisotropic terms in the following:

$$H_J^1 = -\frac{J_2}{4} \sum_{\langle\langle mn \rangle\rangle} 4a_m^\dagger a_m b_n^\dagger b_n - a_m b_n^\dagger b_n^\dagger b_n - a_m^\dagger a_m a_m b_n^\dagger - a_m^\dagger b_n^\dagger b_n b_n - a_m^\dagger a_m^\dagger a_m b_n,$$

$$H_K^1 = K \sum_m a_m^\dagger a_m b_n^\dagger b_n,$$

where $a_m^\dagger(a_m)$ and $b_n^\dagger(b_n)$ are magnon creation (annihilation) operators corresponding to two sublattices $m(n)$. By doing the Fourier transformation, the interacting terms can be written as

$$H_J^1 = -\frac{J_2}{4N} \sum_k 4\bar{\gamma}_{k1-k4} a_{k1}^\dagger a_{k2} b_{k3}^\dagger b_{k4} - \bar{\gamma}_{k1} a_{k1} b_{k2}^\dagger b_{k3}^\dagger b_{k4} - \bar{\gamma}_{k4}^\dagger a_{k1}^\dagger a_{k2} a_{k3} b_{k4}^\dagger$$

$$- \bar{\gamma}_{k1}^\dagger a_{k1}^\dagger b_{k2}^\dagger b_{k3} b_{k4} - \bar{\gamma}_{k4} a_{k1}^\dagger a_{k2}^\dagger a_{k3} b_{k4},$$

$$H_K^1 = \frac{K}{N} \sum_k \bar{\gamma}_{k1-k4} a_{k1}^\dagger a_{k2} b_{k3}^\dagger b_{k4}.$$

As the four-field operators cannot generically be solved exactly, we perform the interacting Green function determined by the effective mean field approximation pictorially represented in Supplementary Fig. 9a.

$$G = G_0 + G_0 \otimes \sum \otimes G.$$

where G_0 is the bared Green function, $\sum$ denotes the self-energy which is evaluated order by order from a perturbative expansion in the magnon-magnon interactions. The $\otimes$ denotes integration over time and space, as well as summation of internal indices. We calculate the Hartree self-energy at first order as shown in Supplementary Fig. 9b, where the Hartree potential is introduced by the effective mean field.

$$a_{k1}^{\dagger}a_{k2}b_{k3}^{\dagger}b_{k4} \approx \langle a_{k1}^{\dagger}a_{k2}\rangle b_{k3}^{\dagger}b_{k4} + \langle a_{k1}^{\dagger}b_{k4}\rangle a_{k2}b_{k3}^{\dagger} + a_{k1}^{\dagger}\langle a_{k2}b_{k3}^{\dagger}\rangle b_{k4} + a_{k1}^{\dagger}a_{k2}\langle b_{k3}^{\dagger}b_{k4}\rangle,$$

$$a_{k1}b_{k2}^{\dagger}b_{k3}^{\dagger}b_{k4} \approx \langle a_{k1}b_{k2}^{\dagger}\rangle b_{k3}^{\dagger}b_{k4} + a_{k1}\langle b_{k2}^{\dagger}b_{k4}\rangle b_{k3}^{\dagger} + \langle a_{k1}b_{k3}^{\dagger}\rangle b_{k2}^{\dagger}b_{k4} + a_{k1}b_{k2}^{\dagger}\langle b_{k3}^{\dagger}b_{k4}\rangle,$$

$$a_{k1}^{\dagger}a_{k2}a_{k3}b_{k4}^{\dagger} \approx \langle a_{k1}^{\dagger}a_{k2}\rangle a_{k3}b_{k4}^{\dagger} + \langle a_{k1}^{\dagger}a_{k3}\rangle a_{k2}b_{k4}^{\dagger} + a_{k1}^{\dagger}a_{k3}\langle a_{k2}b_{k4}^{\dagger}\rangle + a_{k1}^{\dagger}a_{k2}\langle a_{k3}b_{k4}^{\dagger}\rangle,$$

$$a_{k1}^{\dagger}b_{k2}^{\dagger}b_{k3}b_{k4} \approx \langle a_{k1}^{\dagger}b_{k3}\rangle b_{k2}^{\dagger}b_{k4} + \langle a_{k1}^{\dagger}b_{k4}\rangle b_{k2}^{\dagger}b_{k3} + a_{k1}^{\dagger}\langle b_{k2}^{\dagger}b_{k3}\rangle b_{k4} + a_{k1}^{\dagger}\langle b_{k2}^{\dagger}b_{k4}\rangle b_{k3},$$

$$a_{k1}^{\dagger}a_{k2}^{\dagger}a_{k3}b_{k4} \approx \langle a_{k1}^{\dagger}a_{k3}\rangle a_{k2}^{\dagger}b_{k4} + \langle a_{k1}^{\dagger}b_{k4}\rangle a_{k2}^{\dagger}a_{k3} + a_{k1}^{\dagger}\langle a_{k2}^{\dagger}a_{k3}\rangle b_{k4} + a_{k1}^{\dagger}\langle a_{k2}^{\dagger}b_{k4}\rangle a_{k3}.$$

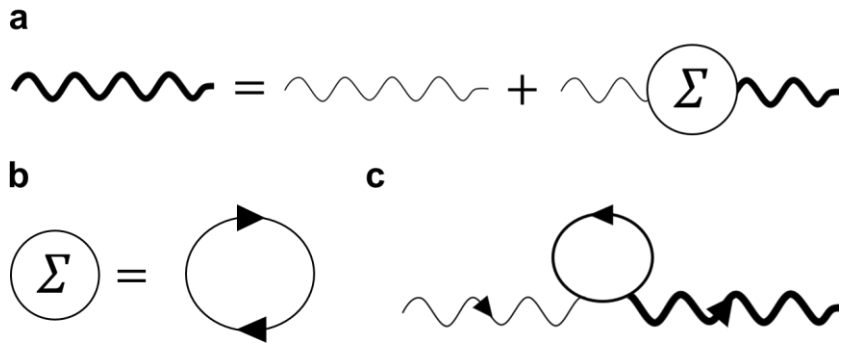

Supplementary Figure 9. One-particle Feynman diagrams of interacting magnons. a, Diagrammatic representation of the Dyson equation for the boson Green function. **b**, Boson self-energy. **c**, First-order Hartree contribution.

The mean-field values are calculated based on the magnon occupancy $\langle n_q\rangle = \frac{1}{e^{\varepsilon_q/k_BT}-1}$. Here $\varepsilon_q \approx 2KS + h_BS + MSq^2$ with $M = \frac{3}{4}J_1 + \frac{9}{2}J_2 + 3J_3$. A single circle of one-particle Feynman

diagram is shown in Supplementary Fig. 9c, where q is the relative momentum from the Γ point. The mean field values can be written as

$$\langle a_q^\dagger a_q\rangle = \langle b_q^\dagger b_q\rangle = \frac{1}{2}\langle n_q\rangle, \langle a_q^\dagger b_q\rangle = \frac{1}{2}e^{-i\phi_q}\langle n_q\rangle, \langle b_q^\dagger a_q\rangle = \frac{1}{2}e^{i\phi_q}\langle n_q\rangle, where\ \phi_q = arg(\gamma_q).$$

Based on the above analysis, we can rewrite the interacting terms as

$$H_J^1 = -\frac{J_2}{2N}\begin{bmatrix} \sum_q \left(|\bar{\gamma}_0| - |\bar{\gamma}_q|\right)\langle n_q\rangle & \sum_q \left(\bar{\gamma}_{k-q}e^{i\phi_q} - \bar{\gamma}_k\right)\langle n_q\rangle \\ \sum_q \left(\bar{\gamma}_{k-q}^\dagger e^{-i\phi_q} - \bar{\gamma}_k^\dagger\right)\langle n_q\rangle & \sum_q \left(|\bar{\gamma}_0| - |\bar{\gamma}_q|\right)\langle n_q\rangle \end{bmatrix},$$

$$H_K^1 = \frac{K}{2N}\begin{bmatrix} \sum_q |\bar{\gamma}_0|\langle n_q\rangle & \sum_q \bar{\gamma}_{k-q}e^{i\phi_q}\langle n_q\rangle \\ \sum_q \bar{\gamma}_{k-q}^\dagger e^{-i\phi_q}\langle n_q\rangle & \sum_q |\bar{\gamma}_0|\langle n_q\rangle \end{bmatrix}.$$

At finite temperatures, thermal fluctuations renormalize magnon dispersion relations, causing a depletion of the static magnetization. The self-energy corrections are calculated from the integration of the first Brillouin zone (BZ), where the Zeeman field produce the Hartree potential energy.

$$N_K = \frac{1}{2}\iint_{BZ}\frac{dq_x dq_y}{e^{\varepsilon_q/k_BT}-1} = \frac{3\sqrt{3}\pi T^2}{128M^2}e^{-\frac{h_B}{k_BT}},$$

$$N_J = -\frac{1}{2}\iint_{BZ}\frac{dq_x dq_y}{e^{\varepsilon_q/k_BT}-1} = -\frac{3\sqrt{3}\pi T^2}{128M^2}e^{-\frac{h_B}{k_BT}},$$

We calculate the self-energy corrections $\sum$ via coefficient N_K when the corresponding Goldstone gap Δ_G is widened by the magnetic field. The field-dependence van Hove singularities (vHS) is modified by N_J as follows

$$\Delta_G = h_B S + 2\left(1 - N_K e^{-\frac{h_B}{k_BT}}\right)KS$$

$$\Delta_{\mathrm{v1}} = 2J_1S + 6J_3S + h_BS + 8\left(1 - N_Je^{-\frac{h_B}{k_BT}}\right)J_2S + 2\left(1 - N_Ke^{-\frac{h_B}{k_BT}}\right)KS$$

$$\Delta_{\mathrm{v2}} = 4J_1S + h_BS + 8\left(1 - N_Je^{-\frac{h_B}{k_BT}}\right)J_2S + 2\left(1 - N_Ke^{-\frac{h_B}{k_BT}}\right)KS$$

3. Dispersion Relations

The magnon dispersion consists of the acoustic and optical branches. The acoustic branch features a gap at the Γ point and a van Hove singularity (vHs) at the M point, reflecting the underlying long-range magnetic order and the RKKY interaction on the Au substrate. We calculate the self-energy corrections ∑ via coefficient N_K when the corresponding Goldstone gap Δ_{G} is widened by the magnetic field.

$$\Delta_{\mathrm{G}} = h_BS + 2\left(1 - N_Ke^{-\frac{h_B}{k_BT}}\right)KS,$$

where $J_1 = 2.12\,meV$, $K = 0.12\,J_1$ and $N_K = 0.07$ accurately determined by the field-dependent evolution of the gap from 0.6 to 1.6 meV. Conversely, the inelastic neutron scattering exhibits $J_1 = 2.01\,meV$ reducing the Goldstone gap as shown in Supplementary Fig. 10a.[2]

We perform the intersection of the acoustic and optical branches at the K point with linear crossing around the Dirac cone, indicating that the magnon velocity remains constant across this region. The fourfold degeneracy at the $K^{\pm} = \left(\frac{2\pi}{3}, \pm\frac{2\pi}{3\sqrt{3}}\right)$ point is a manifestation of the Dirac linear dispersion relation, which is protected by the lattice symmetry and time-reversal symmetry.

$$\Delta_{\mathrm{DM1}} = 3J_1S + 3J_3S + h_BS + 9\left(1 - N_Je^{-\frac{h_B}{k_BT}}\right)J_2S + 2\left(1 - N_Ke^{-\frac{h_B}{k_BT}}\right)KS - 3\sqrt{3}D_zS, \quad (1)$$

$$\Delta_{\mathrm{DM2}} = 3J_1S + 3J_3S + h_BS + 9\left(1 - N_Je^{-\frac{h_B}{k_BT}}\right)J_2S + 2\left(1 - N_Ke^{-\frac{h_B}{k_BT}}\right)KS + 3\sqrt{3}D_zS, \quad (2)$$

where the value of DMI $D_z = 0.08\,J_1$ fixes the topological gap size of 2.7 meV with $\Delta_{\mathrm{DM2}} - \Delta_{\mathrm{DM1}} = 6\sqrt{3}D_zS$, transforming the system into a MCI. Theoretically, the RKKY interaction,

superexchange, and spin-orbit coupling collaborate to induce uniaxial anisotropy and open gaps at Dirac points fitting the rather large DM interaction D_z and anisotropic term K. Moreover, the optical branch typically shows the second vHs at the M point and a maximum at the Γ point with the long-range interaction coefficient increased. We analytically derive the $J_3 = -0.04\,J_1$ for the maximum value of 19.5 meV as follows

$$\Delta_{\max} = 6J_1S + h_BS + 6J_3S + 2\left(1 - N_K e^{-\frac{h_B}{k_BT}}\right)KS.$$

In contrast to the best-fit values, we plot in Supplementary Fig. 10b the theoretical results without the J_3. Two field-dependence vHSs are modified by N_J, contributing to the energy shift of the magnon spectra.

$$\Delta_{\mathrm{v1}} = 2J_1\mathrm{S} + 6J_3S + h_BS + 8\left(1 - N_J e^{-\frac{h_B}{k_BT}}\right)J_2S + 2\left(1 - N_K e^{-\frac{h_B}{k_BT}}\right)KS,$$

$$\Delta_{\mathrm{v2}} = 4J_1S + h_BS + 8\left(1 - N_J e^{-\frac{h_B}{k_BT}}\right)J_2S + 2\left(1 - N_K e^{-\frac{h_B}{k_BT}}\right)KS$$

where $J_2 = 0.15J_1$ and $N_J = 0.13$. We plot in Supplementary Fig. 10c the theoretical results without the J_2.

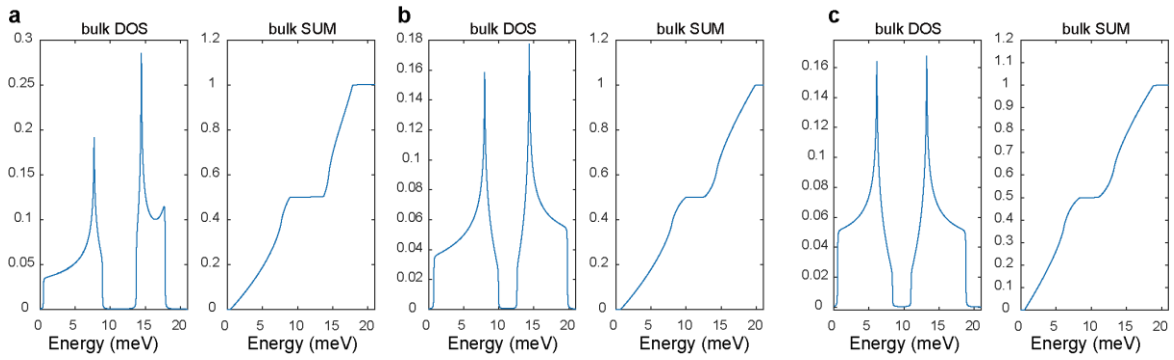

Supplementary Figure 10. Theoretical magnon DOS $\left|d^2I/dV^2\right|$ and the integration $|dI/dV|$. **a**, Comparison with bulk results obtained from INS results.[2] Parameters choices are $J_1 = 2.01meV$,

$J_2 = 0.16meV$, $J_3 = -0.08meV$, $D_z = 0.31meV$ and $K = 0.22meV$. **b**, Comparison with our best-fit values in the absence of the J_3. **c**, Comparison with our best-fit values in the absence of the J_2.

4. Magnon Density of States

In monolayer CrI_3, thermally excited magnons contribute to a redshift of the spectrum related to the magnon density of states (DOS).

$$D(E) = \int \delta(E - \omega_k) d_k^2.$$

where ω_k contain thermal renormalization of the effective exchange couplings. We develop the effective mean-field theory to describe the low-energy dynamics of associated Goldstone gap. Particular in ferromagnets with long-range order, Goldstone modes emerge as gapless excitations around the ground state when continuous symmetries are spontaneously broken. These thermodynamic behaviors are intimately tied to the topological properties which are determined by Eq (1) and (2).

The gap size of $|d^2I/dV^2|$ is determined by the value of DMI, which transforms the systems into a MCI.

For honeycomb ribbons, two gapless boundary states with opposite dispersions emerge within the topological gap. Considering the bulk-edge correspondence, the persistence of edge states are rooted in the unaltered Chern numbers of the bulk. We calculate the edge states in the following for both the zigzag (down) and armchair (up) edges shown in Supplementary Fig. 11.

$$H_{edge} = \sum_{k_x} \psi_{k_x}^{\dagger} H_{k_x} \psi_{k_x}, H_{k_x} = \begin{pmatrix} h & \Delta & \cdots & 0 \\ \Delta^{\dagger} & h & \ddots & \vdots \\ \vdots & \ddots & \ddots & \Delta \\ 0 & \ldots & \Delta^{\dagger} & h \end{pmatrix},$$

where $\psi_{k_x}^{\dagger} = \left(a_{k_x,1}^{\dagger} \quad b_{k_x,1}^{\dagger} \quad a_{k_x,2}^{\dagger} \quad b_{k_x,2}^{\dagger}\right)$.

For the zigzag edge, we have

$$\Delta_{zigzag} = S\begin{pmatrix} 2J_2cos(k_x) - 2D_zsin(k_x) & 0 \\ -J_1 - J_3 & 2J_2cos(k_x) + 2D_zsin(k_x) \end{pmatrix},$$

$$h_{zigzag} = S\begin{pmatrix} \varepsilon_0 - 2J_2cos(2k_x) - 2D_zsin(2k_x) & -2J_1cos(k_x) - 2J_3cos(2k_x) \\ -2J_1cos(k_x) - 2J_3cos(2k_x) & \varepsilon_0 - 2J_2cos(2k_x) - 2D_zsin(2k_x) \end{pmatrix}.$$

For the armchair edge, we have

$$\Delta_{armchair} = S\begin{pmatrix} -4J_2cos\left(\frac{\sqrt{3}}{2}k_x\right) + 4D_zsin\left(\frac{\sqrt{3}}{2}k_x\right) & 0 \\ -J_1 - J_3 & -4J_2cos\left(\frac{\sqrt{3}}{2}k_x\right) - 4D_zsin\left(\frac{\sqrt{3}}{2}k_x\right) \end{pmatrix},$$

$$h_{armchair} = S\begin{pmatrix} \varepsilon_0 - 2J_2cos\left(\sqrt{3}k_x\right) - 2D_zsin\left(\sqrt{3}k_x\right) & -2J_1cos\left(\frac{\sqrt{3}}{2}k_x\right) - 2J_3cos\left(\sqrt{3}k_x\right) \\ -2J_1cos\left(\frac{\sqrt{3}}{2}k_x\right) - 2J_3cos\left(\sqrt{3}k_x\right) & \varepsilon_0 - 2J_2cos\left(\sqrt{3}k_x\right) + 2D_zsin\left(\sqrt{3}k_x\right) \end{pmatrix}.$$

Here $\varepsilon_0 = 3J_1 + 6J_2 + 3J_3$. This topological character is manifested through the existence of robust edge states. The experimental results are approximately fitted via mixing two renormalized edge DOSs with a weight of 0.2 as shown in Supplementary Fig. 11. The width of ribbons is $W = 20$ for both edges.

Although thermally excited magnons contribute to the depletion of magnetization, our calculations highlight the topological characteristics against perturbations and reductions of the

spin stiffness. The localized edge states withstand various defects and impurities, which are immune to disorder and provide a platform for dissipationless transport.

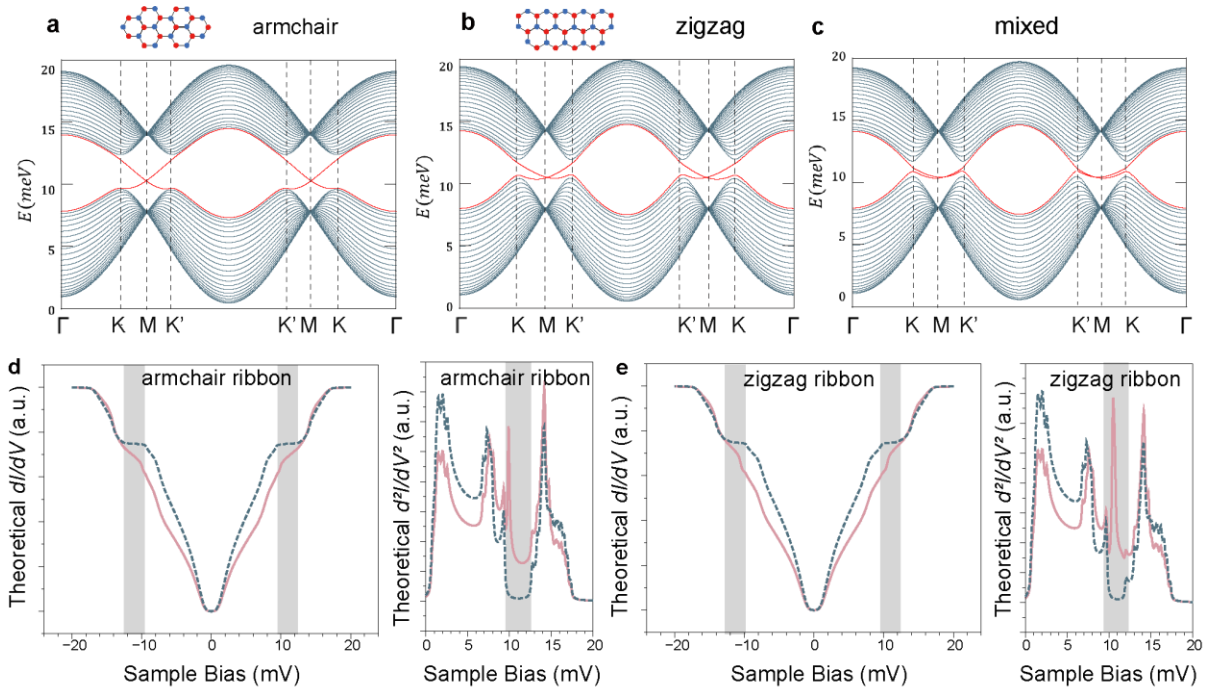

Supplementary Figure 11. Schematics of the open boundary condition. a, The magnon band structure of armchair edge states for a honeycomb ribbon. **b**, The magnon band structure of zigzag edge states for a honeycomb ribbon. **c**, The magnon band structure of mixed edge states for a honeycomb ribbon. The dispersions of the edge states in gaps in Supplementary Fig. 11a to 11c are shown by red curves. **d**, The theoretical dI/dV and d^2I/dV^2 results for the armchair ribbon. **e**, The theoretical dI/dV and d^2I/dV^2 results for the zigzag ribbon.

References

1. Ganguli, S. C. *et al.* Visualization of moiré magnons in monolayer ferromagnet. *Nano Lett.* **23**, 3412–3417 (2023).

2. Chen, L. *et al.* Topological spin excitations in honeycomb ferromagnet CrI_3. *Phys. Rev. X* **8**, 041028 (2018).